Finite Element Simulation of Edge Absorbers for Room Acoustic Applications

Florian Kraxberger[1,*], Eric Kurz[2], Leon Merkel[1], Manfred Kaltenbacher[1] und Stefan Schoder[1]

[1] *Technische Universität Graz, Institut für Grundlagen und Theorie der Elektrotechnik (IGTE), 8010 Graz, Österreich,*

[2] *Technische Universität Graz, Institut für Signalverarbeitung und Sprachkommunikation (SPSC), 8010 Graz, Österreich*

[*] *E-Mail: kraxberger@tugraz.at*

Introduction

Porous absorbent material is often placed in or close to the edge of the room to perform acoustic treatments in rooms for the low-frequency range [1, 2, 3]. This work utilizes a simulation procedure originally introduced in [4] based on the Helmholtz equation, which is solved using the Finite Element (FE) method, as implemented in the FE framework *openCFS* [5, 6]. Thereby, the equivalent fluid model parameters, i.e., complex density and bulk modulus, of the used porous material is obtained with the Johnson-Champoux-Allard-Lafarge (JCAL) model [7]. The parameters of the JCAL model are determined by fitting a reflection coefficient measured in the impedance tube, as described in [8]. The simulated room is modeled with sound-hard boundary conditions and has the same dimensions as the reverberation chamber (RC) at the Building Physics Laboratory at Graz University of Technology[1]. A sketch of the room's geometry is depicted in fig. 1. The edge absorber (EA) is located along one edge of the longest room dimension, colored greenish in fig. 1. Four EA configurations are simulated in total: the empty edge, and the three different configurations EA1 to EA3, as sketched in fig. 2.

Performing the FE simulation in the frequency domain allows for determining the transfer functions (TFs) between sound source and microphone positions. Subsequently, these TFs are compared with those of real reverberation time measurement in the echo chamber. Therewith, it can be shown that the simulation results are in good agreement with the measurements. The FE simulation results predict the sound field in the room, and additionally the simulated sound field in the absorber can be visualized.

Simulation Model

Acoustic wave propagation in the frequency domain is described by the Helmholtz equation
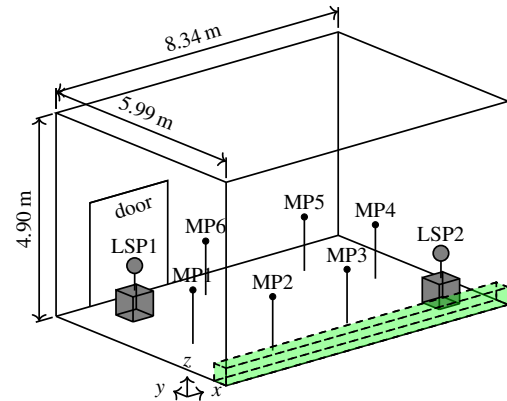
$$\frac{\omega^2}{K}p + \nabla \cdot \left(\frac{1}{\rho}\nabla p\right) = 0 \quad \text{in} \quad \Omega,$$

$$\text{Dirichlet BC:} \quad p = 1\,\text{Pa} \quad \text{at} \quad \boldsymbol{x}_{\text{src}},$$

$$\text{Neumann BC:} \quad \nabla p \cdot \boldsymbol{n} = 0 \quad \text{at} \quad \partial\Omega,$$

$$(1)$$

where $\omega = 2\pi f$ is the angular frequency, $\boldsymbol{x}$ is a point in the computational domain Ω, $\partial\Omega$ is the boundary of Ω, $\boldsymbol{n}$ is the outward pointing normal vector of $\partial\Omega$, K is the bulk modulus, ρ is the material density, $\boldsymbol{x}_{\text{src}}$ is the source position, and p is the acoustic pressure, i.e., the

Figure 1: Sketch of geometry with microphone (MP1—MP6) and loudspeaker positions (LSP1, LSP2). The volume into which the EA configurations are inserted is colored green [4, fig. 4b].
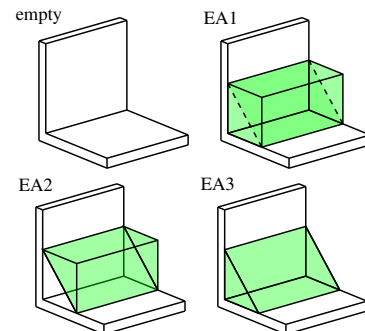
Figure 2: Simulation configurations empty, EA1, EA2, and EA3. The absorbent material is colored greenish [4, fig. 1b].

solution quantity. The model is excited by a constant Dirichlet boundary condition (BC) at a source position $\boldsymbol{x}_{\text{src}}$. The walls are modeled sound-hard, i.e., a homogeneous Neumann BC is used at the domain boundary $\partial\Omega$. Bulk modulus K and density ρ depend on frequency ω and location $\boldsymbol{x}$, i.e.,

$$K = \begin{cases} K_0 & \text{for } \boldsymbol{x} \in \Omega_{\text{air}} \\ K_{\text{abs}}(\omega) & \text{for } \boldsymbol{x} \in \Omega_{\text{abs}} \end{cases},$$

$$\rho = \begin{cases} \rho_0 & \text{for } \boldsymbol{x} \in \Omega_{\text{air}} \\ \rho_{\text{abs}}(\omega) & \text{for } \boldsymbol{x} \in \Omega_{\text{abs}} \end{cases}.$$

$$(2)$$

Thereby, $K_0 = 141\,855\,\text{N/m}^2$ and $\rho_0 = 1.2305\,\text{kg/m}^3$ are the bulk modulus and density of air at the measurement temperature, respectively [4].

Equivalent Fluid Model for Porous Material

$K_{\text{abs}}(\omega)$ and $\rho_{\text{abs}}(\omega)$ are the equivalent bulk modulus and equivalent density in the absorber region Ω_{abs}, for which

Table 1: Initial parameters $\boldsymbol{\theta}_{\mathrm{JCAL,init}}$ and optimized parameters $\boldsymbol{\theta}_{\mathrm{JCAL,opt}}$ as a result of the fitting algorithm.

|	ϕ	k_0'	Λ	Λ'	σ	α_∞	reference
$\boldsymbol{\theta}_{\mathrm{JCAL,init}}$	0.994	$27 \cdot 10^{-10}\,\mathrm{m}^2$	$92\,\mu\mathrm{m}$	$197\,\mu\mathrm{m}$	$10\,934\,\mathrm{Ns/m}^4$	1.04	[9, tab. 1]
$\boldsymbol{\theta}_{\mathrm{JCAL,opt}}$	0.96548	$39.52 \cdot 10^{-10}\,\mathrm{m}^2$	$125.8\,\mu\mathrm{m}$	$284.4\,\mu\mathrm{m}$	$12\,844\,\mathrm{Ns/m}^4$	0.8304	[4, tab. 2]

the JCAL model is used:

$$K_{\mathrm{abs}}(\omega) = \frac{\gamma p_0/\phi}{\gamma - (\gamma-1)\left[1 - \mathrm{j}\frac{\kappa A}{k_0' C_{\mathrm{p}}}\sqrt{1 + \mathrm{j}\frac{4 k_0'^2 C_{\mathrm{p}}}{\kappa \Lambda'^2 \phi A}}\right]^{-1}},$$

$$\rho_{\mathrm{abs}}(\omega) = \frac{\alpha_\infty \rho_0}{\phi}\left[1 + \frac{\sigma A}{\mathrm{j}\alpha_\infty}\sqrt{1 + \mathrm{j}\frac{4\alpha_\infty^2 \eta_0}{\sigma^2 \Lambda^2 \phi A}}\right], \quad (3)$$

where $A = \phi/(\omega\rho_0)$. The JCAL model uses the following six material-dependent parameters: open porosity ϕ, static airflow resistance σ, high-frequency limit of the tortuosity α_∞, viscous characteristic length Λ, thermal characteristic length Λ', and static thermal permeability k_0' [7, 8]. The constitutive constants in the JCAL model are the dynamic viscosity $\eta_0 = 18.232 \cdot 10^{-6}\,\mathrm{kg/(m \cdot s)}$, thermal conductivity $\kappa = 25.684 \cdot 10^{-3}\,\mathrm{W/(m \cdot K)}$, isentropic exponent $\gamma = 1.4$, the ambient air pressure $p_0 = 100\,325\,\mathrm{Pa}$, and the specific heat of air at constant ambient pressure $C_{\mathrm{p}} = 1006.825\,\mathrm{J/(kgK)}$ [4].

To obtain the six parameters of the JCAL model as defined in eq. (3), a genetic fitting algorithm has been used as described in [8], with the initial parameters from [9, tab. 1]. In the specified fitting range between 100 Hz and 250 Hz, the algorithm minimizes the error between the computed reflection coefficient with that one measured in the impedance tube, as depicted in fig. 3. Initial and final values, i.e., the result of the genetic fitting algorithm, are listed in tab. 1. The resulting frequency dependent complex-valued equivalent density and bulk modulus are directly used as input quantities in the FE software *openCFS* [6].
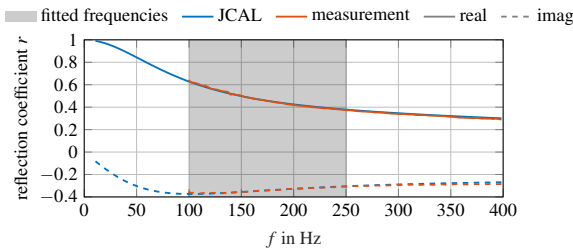
Figure 3: Measured and fitted reflection coefficients $r_{\mathrm{meas}}(f)$ and $r_{\mathrm{JCAL}}(f)$ [4, fig. 2].

Spatial Discretization
In fig. 4, the frequency dependence of the wavelengths in the porous medium $\lambda_{\mathrm{abs}} = \sqrt{K_{\mathrm{abs}}(\omega)/\rho_{\mathrm{abs}}(\omega)} \cdot 2\pi/\omega$ and air $\lambda_0 = \sqrt{K_0/\rho_0} \cdot 2\pi/\omega$ is depicted. While the wavelength in air is real-valued, the computed wavelength in the absorber is complex-valued due to the complex-valued equivalent fluid parameters $K_{\mathrm{abs}}(\omega)$ and $\rho_{\mathrm{abs}}(\omega)$, resulting in a dispersive behavior in the porous medium. In air, the upper frequency limit of interest ($f_u = 200$ Hz) results in a lower wavelength bound of $\lambda_0(f_u) = 1.7$ m, and in the porous material $\lambda_{\mathrm{abs}}(f_u) = 0.5$ m. A rule of
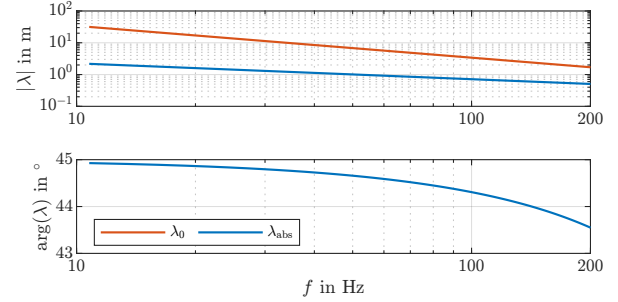
Figure 4: Acoustic wavelengths in air $\lambda_0 \in \mathbb{R}$ and absorber medium $\lambda_{\mathrm{abs}} \in \mathbb{C}$.

thumb for discretizing a domain with second-order Lagrangian elements is to use six elements per wavelength [5]. Due to the different wavelengths in air and absorber volumes depicted in fig. 1, different element sizes are used for each volume connected with a nonconforming interface with Nitsche-type mortaring [6, 10], as depicted in fig. 5. For selecting the appropriate discretization, a grid convergence study has been performed, which is documented in [4].
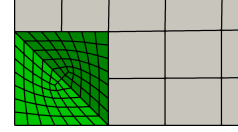
Figure 5: Detail view of the cross-section in the yz-plane through the nonconforming meshes. The absorber volumes are green, and the air volume is gray [4, fig. 3(b)].

Validation Procedure
The FE model has been validated using TFs obtained from twelve impulse response measurements using six microphone positions (MP1 to MP6) and two loudspeaker positions (LSP1, LSP2), as depicted in fig. 1. The measured TFs are compared to simulated TFs evaluated using the FE model at hand. After equalizing the measurements with the inverse frequency response obtained from the loudspeaker data sheet, a level correction was applied to the simulations. The data processing is documented in [4]. Exemplarily, the TFs from LSP1 to MP1 for all configurations are depicted in fig. 6. From fig. 6, it is visible that simulated and measured TFs are in good agreement. Due to discrepancies in frequency resolution between simulations and measurements, a third-octave averaging is introduced for the TFs, resulting in the third-octave band averaged TFs as depicted in fig. 7. The measured TFs are compared to FE simulated TFs by determining the error between the third-octave band averaged TFs, as described in [4], resulting in the third-octave band averaged error

$$Err_{L_p} = \frac{1}{N_{f_m}} \sum_{f_{\mathrm{m}} \in \mathcal{F}} \left| \bar{L}_{p,\mathrm{meas}}(f_{\mathrm{m}}) - \bar{L}_{p,\mathrm{sim}}(f_{\mathrm{m}}) \right|, \quad (4)$$
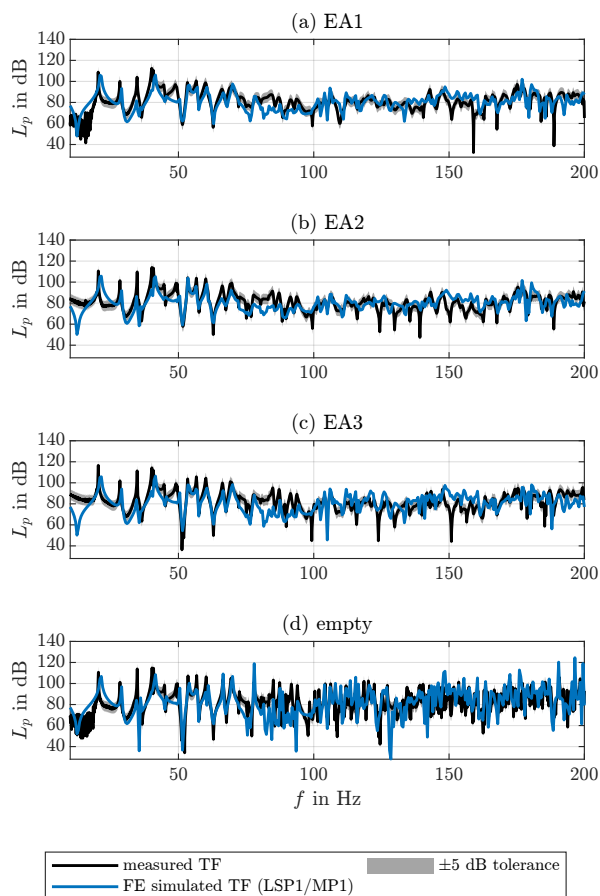
**Figure 6:** Comparison of measured and simulated TF between LSP1 and MP1 for all configurations.

for each TF of each configuration, depicted in fig. 8. Thereby, $\mathcal{F}$ is the set of all third-octave band center frequencies f_m between 20 Hz and 200 Hz, and $N_{f_m} = 9$. Further error quantification can be performed by averaging the error values Err_{L_p} across MP-LSP combinations, resulting in the averaged third-octave band averaged error $\bar{Err}_{L_p}$, which is scalar and only dependent on the configuration. Values of $\bar{Err}_{L_p}$ are included in fig. 8.

Field Results

The FE model is used to visualize the pressure field in both air and absorber volumes. The pressure field resulting from the four EA configurations (cf. fig. 2) is depicted in figure 9. It is clearly visible from fig. 9(a), that at 66.5 Hz, the empty configuration has a pronounced modal field. For configurations EA1 and EA2, this modal field is damped and distorted significantly, see fig. 9(b) and (c), respectively. For configuration EA3, the acoustic field retains its modal characteristic, but it is damped, as depicted in fig. 9(d).

Conclusion

The presented FE model is able to simulate the empty RC as well as three EA configurations with a satisfying degree of accuracy ($\bar{Err}_{L_p}$ ranges from 3.25 dB for the empty RC to 4.11 dB for EA3). A main consequence of applying EA1 or EA3 to a RC is an effect on the low-frequency modal field. The acoustic wave propagation is damped in the porous medium, which results in a dis-
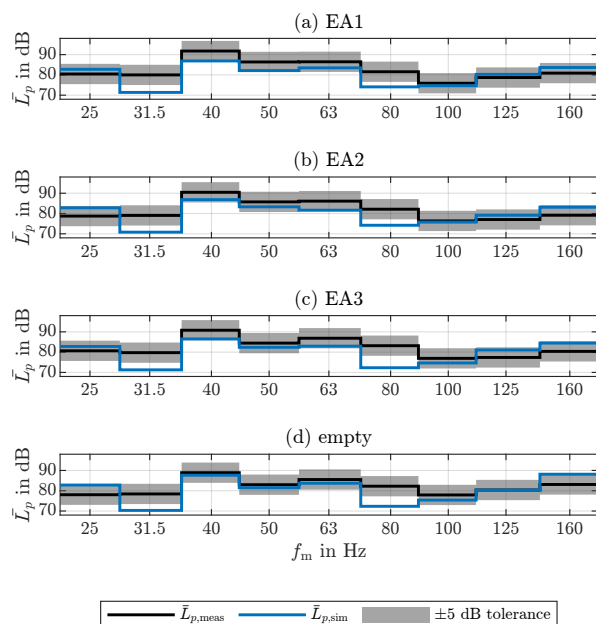
Figure 7: Third-octave band averaged TF $\bar{L}_{p,\mathrm{meas}}(f_\mathrm{m})$ of measurement and $\bar{L}_{p,\mathrm{sim}}(f_\mathrm{m})$ of FE simulation from LSP1 to MP1.
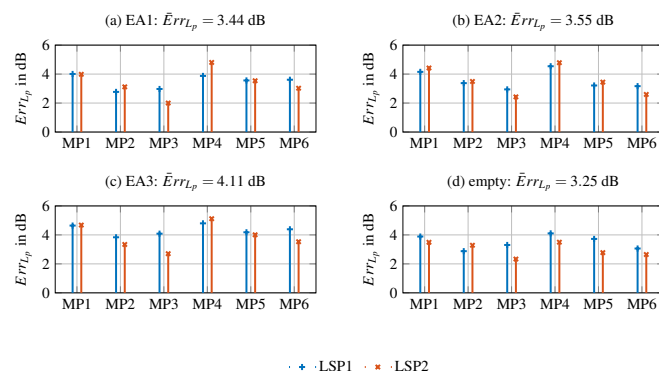
Figure 8: Third-octave band error Err_{L_p} for all configurations and MP-LSP combinations. The averaged error measure $\bar{Err}_{L_p}$ is obtained by averaging Err_{L_p} across LSP/MP-combinations for each configuration. [4, Fig. 7]

torted modal field in the whole RC.

The presented model helps to gain knowledge about the EA. It is a promising tool for further investigations of the effect of EA on the acoustic field using numerical methods. These may include, e.g., investigations on the nonlinear eigenvalue problem of room acoustics with EA, or further validations using acoustic pressure measurements in proximity to the EA. Consequently, this can help acoustic engineers decide on the best absorber type for a specific acoustic problem based on a fundamental understanding of the physical principles behind different types of EA.

Acknowledgment

References

[1] H. V. Fuchs and J. Lamprecht. Covered broadband absorbers improving functional acoustics in commu-

(a) empty

(b) EA1

(c) EA2

(d) EA3
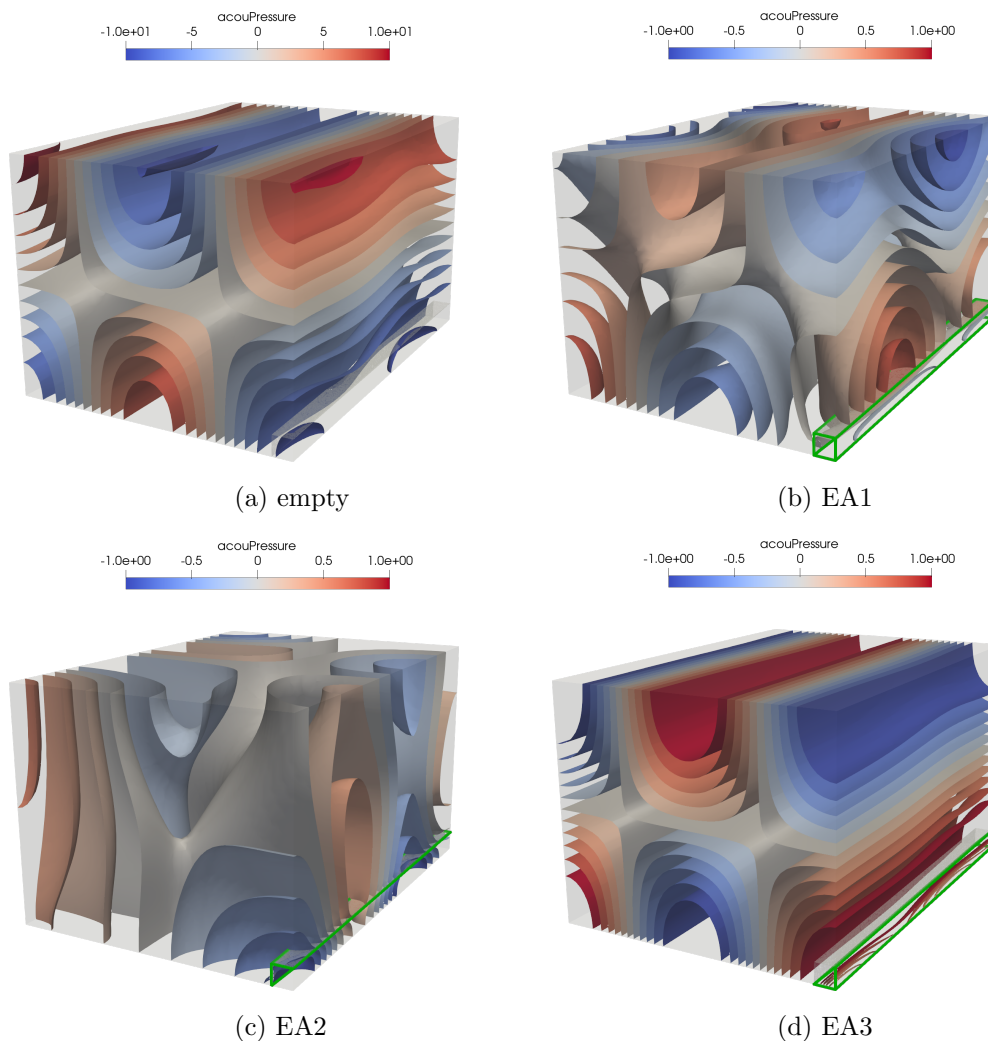
Figure 9: Isosurfaces of the sound pressure field at 66.5 Hz for the empty echo chamber as well as the three EA configurations.

nication rooms. *Appl. Acoust.*, 74(1):18–27, 2013. `doi:10.1016/j.apacoust.2012.06.004`.

[2] E. Kurz, D. Reisinger, W. Weselak, and G. Graber. The edge absorber as a modal brake. In *Proc. of Forum Acusticum*, pages 1745–1752, Lyon, France, December 2020. `doi:10.48465/fa.2020.0574`.

[3] E. Kurz, G. Graber, and W. Weselak. Systematische Untersuchungen zur Funktionsweise des Kantenabsorbers als „Modenbremse". *Elektrotech. Inf.*, 138(3):162–170, 2021. `doi:10.1007/s00502-021-00878-1`.

[4] F. Kraxberger, E. Kurz, W. Weselak, G. Kubin, M. Kaltenbacher, and S. Schoder. A validated finite element model for room acoustic treatments with edge absorbers. *Preprint submitted to Acta Acust.*, February 2023. `doi:10.48550/arXiv.2302.07527`.

[5] M. Kaltenbacher. *Numerical Simulation of Mechatronic Sensors and Actuators: Finite Elements for Computational Multiphysics*. Springer, Berlin–Heidelberg, third edition edition, 2015. `doi:10.1007/978-3-642-40170-1`.

[6] S. Schoder and K. Roppert. openCFS: Open source finite element software for coupled field simulation –

part acoustics, 2022. `doi:10.48550/ARXIV.2207.04443`.

[7] D. Lafarge, P. Lemarinier, J. F. Allard, and V. Tarnow. Dynamic compressibility of air in porous structures at audible frequencies. *J. Acoust. Soc. Am.*, 102(4):1995–2006, 1997. `doi:10.1121/1.419690`.

[8] S. Floss, F. Czwielong, M. Kaltenbacher, and S. Becker. Design of an in-duct micro-perforated panel absorber for axial fan noise attenuation. *Acta Acust.*, 5:24, 2021. `doi:10.1051/aacus/2021015`.

[9] D. Li, D. Chang, and B. Liu. Diffuse sound absorptive properties of parallel-arranged perforated plates with extended tubes and porous materials. *Materials*, 13:1091, March 2020. `doi:10.3390/ma13051091`.

[10] M. Kaltenbacher and S. Floss. Nonconforming finite elements based on nitsche-type mortaring for inhomogeneous wave equation. *J. Theor. Comput. Acoust.*, 26(03):1850028, 2018. `doi:10.1142/S2591728518500287`.